JAST. Vol. 9, No. 1, pp 37-48

JAST
Journal of Aerospace Science and Technology

Helicopter Rotor Airloads Prediction, Using CFD and Flight Test Measurement in Hover Flight

D. Hassanzadeh[1] and A.R. Mostofizadeh[2]

An implicit unsteady upwind solver including a mesh motion approach was applied to simulate a helicopter including body, main rotor and tail rotor in hover flight. The discretization was based on a second order finite volume approach with fluxes given by the Roe's scheme. Discretization of Geometric Conservation Laws (GCL) was devised in such a way that the three-dimensional flows on arbitrary moving grids could be solved. The accurate geometric representation together with the flexibility required for grid displacement was achieved by using a tetrahedral grid. First, the numerical methodology was validated through experimental test data; then, our supposed helicopter configuration was utilized. At the same time, the main rotor loading measurements were done through flight tests. Two methods of moving reference frame (MRF) and viscous/inviscid Dynamic Mesh were compared resulting in robustness of Dynamic Mesh approach. Ultimately, our calculations yielded valid solutions to the blade loading and wake structure.

***Keywords**: CFD, Dynamic Mesh, Moving Reference Frame, Flight Test*

1 Introduction

The helicopter rotor wake is among the most complex fluid dynamic structures being three dimensional and in many cases unsteady. The accurate calculation of the aerodynamic forces on the rotor requires a correct prediction of the vortex wake, including the blade trailing wake as well as the interaction of the tip vortex of one blade with the following blade. The generation of the free wake and its interaction with the blade make the helicopter aerodynamic computation extremely complex [1]. The computational methods for calculating helicopter rotor flow fields can be divided into two types: integral equation methods (panel methods) and finite-difference/finite-volume methods. Integral equation methods for both incompressible and compressible rotor flows were developed by several investigators [2-6]. These methods are able to treat the rotor blade and vortex wake accurately and efficiently. However, they are restricted to linear, low-speed, subsonic flows. This is a very serious limitation because modern rotor blades operate in the transonic regime, where the nonlinear compressibility is important and shocks can exist in the flow field.

Finite-difference/finite-volume methods based on the full-potential [7-9], Euler [10-13] and Navier-Stokes (NS) [14] equations with a single grid for rotor flow fields were developed during the past few years, while more recently the calculations are mainly concerned with various NS equations. The compressible Navier-Stokes equations permit creation of the regions of the flow across which the pressure and velocities are nearly discontinuous; these regions are termed shock waves. Finite-difference methods based on Taylor series approximations are inaccurate in these regions and the convective terms in the governing equations written in a conservative form must be treated with care. Finite-volume schemes are particularly useful for handling shocks since no derivatives appear in the equations [15]. However, numerical methods contain inherent numerical dissipation which depends on the local grid size and the order of the spatial accuracy of the scheme. Accurate capturing of the rotor wake requires several grid points inside the vortex core to prevent the tip vortex diffusion and to maintain its strength.

Hybrid grid topology, including structure grids in near wall region and flexible unstructured grid away from the blade to keep grid density low, has a significant role in minimizing computer resources. So, to distribute the grid points for solution properly, we have used hybrid grid topology.

1. (Corresponding Author), Iran Aircraft Manufacturing Company, Isfahan, Iran
2. Malek-Ashtar University of Technology, Isfahan, Iran, Eng_hassanzadeh@yahoo.com

An implicit steady/unsteady finite-volume, upwind solver, including mesh motion capability, is applied to simulate a helicopter in hover flight with a design tip Mach number of 0.69. Two methods of moving reference frame (MRF) and Dynamic Mesh have been used in this simulation. For Dynamic Mesh solution, a numerical scheme that rigorously addresses the discretization of Geometric Conservation Laws (GCL) is used so that three-dimensional flows can be solved on arbitrarily moving grids. Also, two groups of mesh motion methods, including smoothing methods and local remeshing methods, are used to update the unstructured volume mesh in the deformable regions subject to the motion defined at the boundaries. Using the remeshing method, cells are marked based on cell skewness and minimum and maximum length scales as well as an optional sizing function. These marked cells start remeshing if they meet greater skewness than a specified maximum skewness or a smaller length scale than a specified minimum length scale or a larger length scale than a specified maximum length scale.

To allow the use of very fine meshes, and hence, better representation of the flow physics, the problem was run on Parallel Processing Center using the meshes of density up to 3 million cells.

2 Governing Equation

Steady (for MRF approach) and unsteady (for Dynamic Mesh approach) formulations of the flow-solver are presented below.

2.1 Steady formulation

problem is a helicopter with a main/tail rotor as a rotating zone and a body as a stationary zone. In this case, we must break up the model into multiple fluid/solid cell zones, with interface boundaries separating the zones. The zones which contain the moving components can, then, be solved using the moving reference frame equations, whereas the stationary zones are solved with the stationary frame equations. At the interfaces between the cell zones, a local reference frame transformation is performed to enable flow variables in one zone to be used to calculate the fluxes at the boundary of the adjacent zone.

Hover simulation requires a rigid but rotating grid. In the rotating zone, equations are transformed to a blade-fixed rotating reference frame as in this frame the hover case is a steady problem. Hence, absolute velocities are used. If the frame rotates with the angular velocity $\omega=[\Omega x,\Omega y,\Omega z]T$, and the absolute velocity vector in the rotating frame is denoted by $qr=[ur,vr,wr]T$, the result-

$$\frac{d}{dt}\int_{V_r} U_r dV_r + \int_{\partial V_r} F_r.n_r dS_r + \int_{V_r} G_r dV_r = 0, \qquad (1)$$

$$U_r = \begin{bmatrix} \rho \\ \rho u_r \\ \rho v_r \\ \rho w_r \\ E \end{bmatrix}, F_r = \begin{bmatrix} \rho[q_r - (\omega \times r)] \\ \rho u_r[q_r - (\omega \times r)] + Pi_r \\ \rho v_r[q_r - (\omega \times r)] + Pj_r \\ \rho w_r[q_r - (\omega \times r)] + Pk_r \\ E[q_r - (\omega \times r)] + Pq_r \end{bmatrix}, \qquad (2)$$

$$G_r = \begin{bmatrix} 0 \\ \rho(\omega \times q_r)i_r \\ \rho(\omega \times q_r)j_r \\ \rho(\omega \times q_r)k_r \\ 0 \end{bmatrix}.$$

In above equations, Gr is the source term resulting from the transformation, and $r=[xr,yr,zr]T$ is the coordinate vector. Here, grid speeds are constant, i.e. the coordinate vector is constant in the rotating frame. The equation set is closed by:

$$P = (\gamma - 1)\left[E - \frac{\rho}{2} q_r^2\right]. \qquad (3)$$

A cell-centered, finite-volume discretization together with the standard upwind Roe flux-difference splitting of inviscid flux vector Fr, appearing in Equation (2), is used to solve the above integral form of the Euler equations (Equation 1).

2.2 Unsteady formulation

The unsteady formulations of governing equations are presented as follows:

$$\frac{d}{dt}\int_V UdV + \int_{\partial V} F.nds = 0 \qquad (4)$$

$$U = \begin{bmatrix} \rho \\ \rho u \\ \rho v \\ \rho w \\ E \end{bmatrix}, \qquad (5)$$

$$F_r = \begin{bmatrix} \rho[q_r - (\omega \times r(t) + r_t(t))] \\ \rho u[q_r - (\omega \times r(t) + r_t(t))] + P_r \\ \rho v[q_r - (\omega \times r(t) + r_t(t))] + P_r \\ \rho w[q_r - (\omega \times r(t) + r_t(t))] + Pk \\ E[q - (\omega \times r(t) + r_t(t))] + Pq \end{bmatrix}$$

The coordinate vector r (t) is time dependent in the fixed axis system in which we have:

$$r(t) = [R(\Psi)]r(0) \tag{6}$$

where, [R (Ψ)] is the time-dependent rotation matrix in which Ψ is the azimuth position, and so Ψ=ωt. The ω×r (t) term is due to the rigid rotation, but there is also the grid velocity associated with grid deformation, and this is the r (t) term in the above equation. The time derivative term in Eq. 4 was written using a first-order backward difference formula and convective flux vector evaluated by second order upwind Roe flux-difference splitting [16].

In order for fluid dynamics conservation laws that use body conforming coordinate transformations to maintain global conservation, spatial and temporal grid metrics must satisfy certain geometric identities. In differential or integral form, the restriction is similar to mass conservation and is known as the Geometric Conservation Law (GCL) [17]. The GCL is related to the ability of a numerical scheme to preserve the state of a uniform flow. Grid metrics with this property are called free-stream preserving. Satisfying these conditions may improve the stability and spatial and/or temporal accuracy of the CFD algorithm.

During this simulation, two groups of mesh motion methods, including smoothing methods and local remeshing methods, are used to update the unstructured volume mesh in the deformable regions subject to the motion defined at the boundaries. Using the remeshing method, cells are marked based on cell skewness and minimum and maximum length scales as well as an optional sizing function. These marked cells start remeshing if they meet greater skewness than a specified maximum skewness or a smaller length scale than a specified minimum length scale or a larger length scale than a specified maximum length scale.

3 Domain Setup for Two Cases

Here, we have taken two geometries with two different approaches under study. The first case of simulation is made for the experimental hovering rotor of Tung and Caradona [18], simply including two untwisted blades with +8 deg angle of attack. This case is selected for validation of CFD algorithms. Calculation for the second case is made for a helicopter including a main/tail rotor and body configuration for which experimental measurements were done in HESA Company. A proper computational grid is made for each case. For the first case, we made an inner cylindrical region with dense meshes nearly around the blades and an outer cylindrical region including growing meshes with spanwise far-field (radius of sector) at 80 chords, the upper boundary at 80 chords and lower boundary at 150 chords. The inner (smaller) region is named rotating zone and the outer one is called stationary zone. The interfaces between these two zones were applied as “interior”. A grid dependency study was performed and mesh densities of 0.8, 1.5, and 3 and 6 million cells were generated using blade surface adaption. For the second case, we made three regions for the main rotor, tail rotor as rotating zones and the body as a stationary zone. The domain extending for this case is the same as the former one based on chord length. The pressure boundary condition was applied for far-field, inlet and out-let boundaries and the no-slip condition was used for rotating blades.

4 Parallel Implimentation

To allow the use of very fine meshes, and hence, better representation of the flow physics, the problem was parallelized by partitioning the computational domain into several subdomains. Communication of the data between each processor was achieved by using the MPI (Message Passing Interface) library. For the present cell-centered scheme, the data communication involve flow variables at the nodes, at the face centroids, and at the adjacent cell centroids of the subdomain boundary. The partitioning was performed using the MeTiS library by considering the number of cells assigned to each processor to achieve load balancing. Grid densities of 0.4, 1.5, 3 and 6 million cells were selected using 1 to 36 computational nodes. A higher density of grid is needed for capturing the tip vortices accurately but 1.5 million volume cells, including viscous and inviscid cells, seem to give appropriate results for load calculations on rotating blades. The total computational time required for the converged solution for this grid density is about 120 hours using 16 processors for Dynamic Mesh approach and about 32 hours using 8 processors for MRF. An excessive number of iterations were used to obtain a fully-converged solution.

5 Computational Details for the First Case

Those calculations are made for the experimental hovering rotor of Caradonna and Tung [18]. The experimental model has a two-bladed, untwisted, rigid rotor. The blades are made of an NACA 0012 airfoil section with a rectangular planform and an aspect ratio of 6.0. One transonic and one subsonic hovering flight conditions are chosen from the experimental data in the present calculations: 1) tip Mach number Mtip=0.877, collective pitch angle θc=+8 deg and 2) Mtip=0.44, θc =+8 deg. Two approaches of inviscid MRF and viscous/inviscid Dynamic Mesh are used to calculate the pressure distribution on different sections. According to relatively low accuracy of inviscid calculation, we have also presented the turbulent solution of the flow field using the eddy-viscosity transport model of Spallart-Allmaras equipped with a proper wall function. Appropriate grid

points for turbulent analysis are made considering y+ so each wall-adjacent cell's centroid is located within the log-law layer (30<y+<300). A value close to the lower bound (y+≈30) is most desirable. Fig's. 1-4 show the blades configuration, surface grids on blade, surface grids on domain and sectional grids of the blade, respectively.

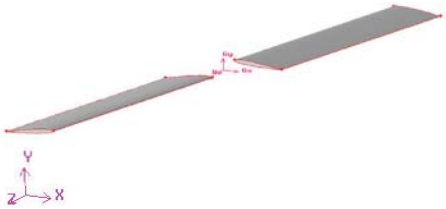

Figure 1. Blades Configuration of the Experimental Hovering Rotor of Caradonna and Tung.

Figure 2. Surface Grids on Blade at θ_C=+8 deg and MTIP=0.877.

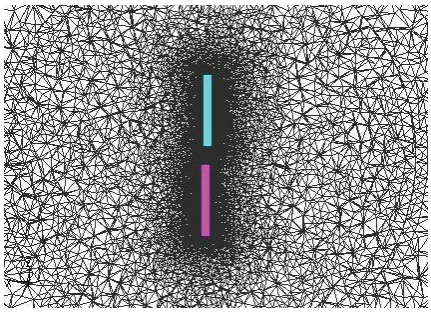

Figure 3. Surface Grids on Domain along the Blades Surface at θ_C=+8 deg and MTIP=0.877.

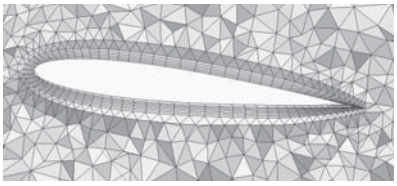

Figure 4. Sectional View of Computational Grids at X/C=0.89.

6 Results and Discussion of First Case

A view of the computed flow field is shown in Fig.5 which also includes vortex sheets moving downward with induced velocity. Induced velocity variation along the blade for both inviscid MRF and Dynamesh (Dynamic mesh) approaches is shown in Fig. 6 at different azimuth angles. According to physical concepts, we are going to have tip and root vortices at the ends of the rotating blade causing upward flow motion. Here, untwisted blades were selected to keep the tip region well loaded so as to produce a relatively strong tip vortex. Considering initial blades at 90 Deg. azimuth angle, Fig's. 6-7 represent the robustness of Dynamic Mesh method in capturing tip and root vortices. As seen in this figure, induced velocity takes positive value near the root and tip regions by Dynamic Mesh solution which confirms the upward flow motion.

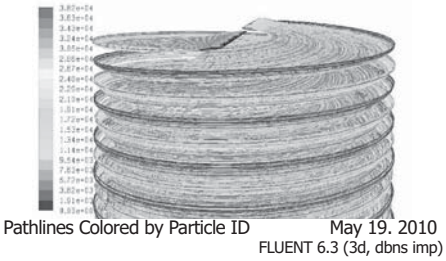

Figure 5. Vortex Sheets Generated from Rotating Blades.

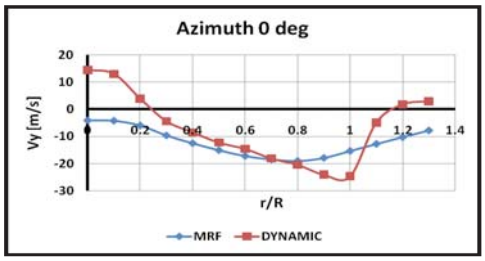

(a)

Figure 6. Induced Velocity Distribution along Blade at 45, 90 and 180 deg Azimuth Angle.

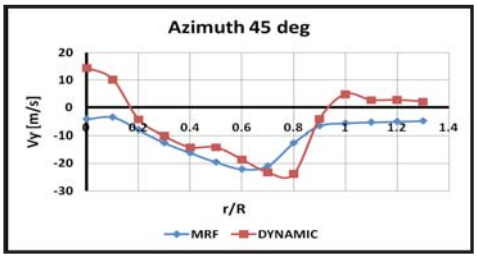

(b)

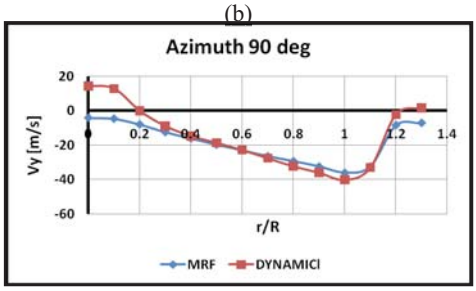

(c)

Figure 6. Cont'd.

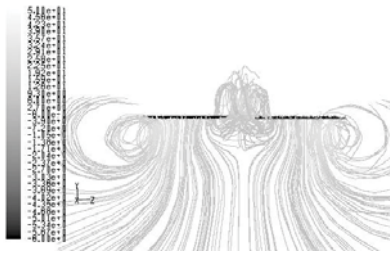

Figure 7. Calculated Flow Field around Rotating Blades at θ_C=+8 deg and MTIP=0.877.

As mentioned above, Fig. 6 (c) indicates the induced velocity at the same azimuth with an advancing blade. At this position, we have maximum induced velocity. By getting far away from the blade (increasing vortex age), induced velocity variation along the blade is damped out until it gets to 45 azimuth angle. Therefore, in a case of two blades, induced velocity at 45 deg aft of the blade instantaneous position gets its minimum value. From this point on, induced velocity is influenced by the flow field and may start to get its maximum value up to 90 deg due to dynamic features. For better understanding, induced velocity distribution along the blade is given Fig. 8 in several azimuth angles calculated by Dynamic Mesh method. It is obvious that, with the phase angle of 45 deg, induced velocity is minimized periodically. This can be helpful in helicopter body vibration analysis as there is a periodic download in helicopter operations.

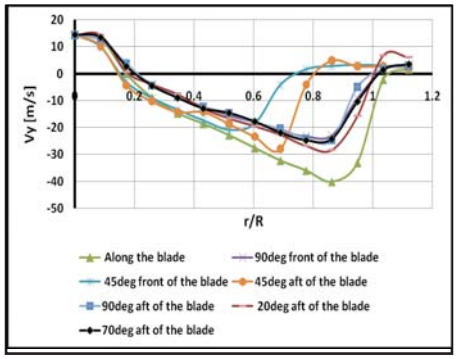

Figure 8. Induced Velocity Distribution along Blade in Different Positions Relative to Blade.

For comparison purposes, the predicted surface pressure coefficients are compared with the Tung and Caradona experiment [18]. Two MRF and Dynamic Mesh methods with an extra turbulent solution for Dynamic Mesh (to see viscous effects and get more accurate results) are presented for two flow regimes with Mach numbers of 0.44 and 0.877 (Fig's. 9-10). Dynamic Mesh method together with the eddy-viscosity transport model shows acceptable results comparing with experimental data. The viscous simulation predicts slightly less blade loading than that of the inviscid calculation mostly at inboard of the blade. In fact, each rotating blade generates a wake structure composed of a vortex sheet and tip vortex. This shed vortex interacts with the second blade, resulting in a pressure change on the blade. The interpretation of this phenomenon is that the blade has different angle of attack than its geometrical one. By capturing the wake structures with more details, we can predict the accurate aerodynamics of the rotating blades. For fix-wing, as we don't have blade vortex interaction, existing wake will not be very significant. In the rotating blade case, the flow is mostly vortical, so shear layers come to existence.

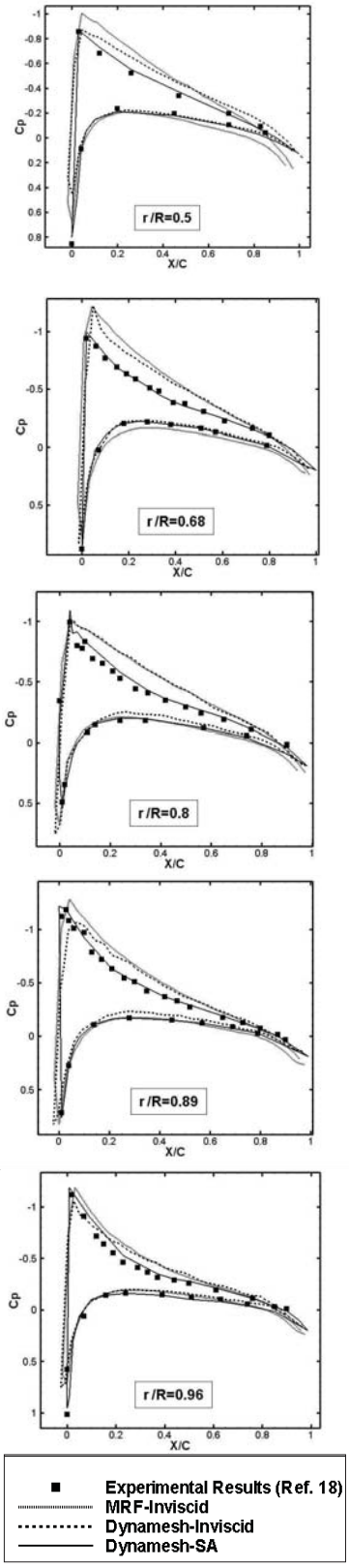

Figure 9. Pressure Coefficient Distributions on the Blade. M_{tip}=0.44 and θ_C=+8 deg.

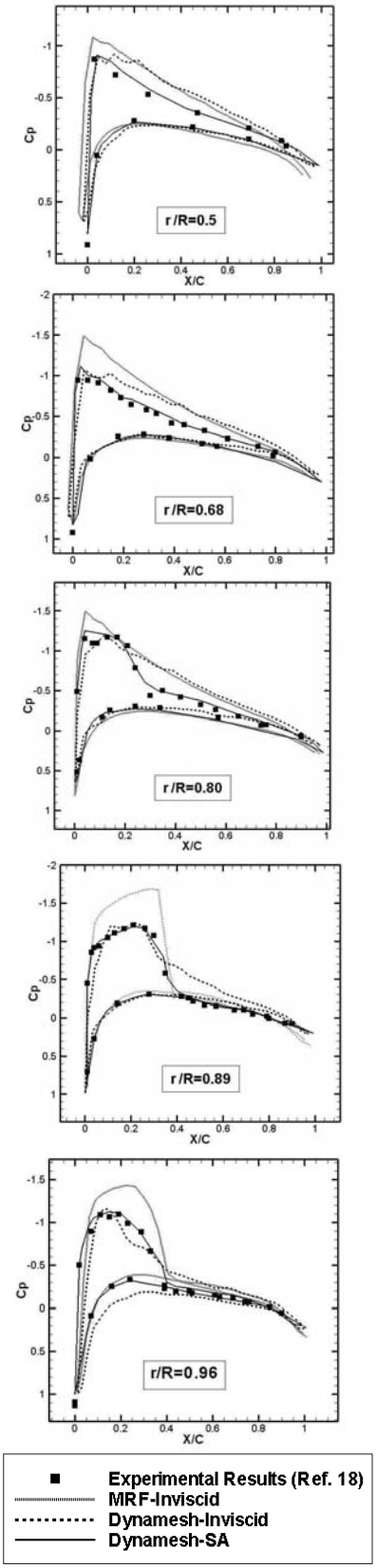

Figure 10. Pressure Coefficient Distributions on the Blade. M_{tip}=0.877 and θ_C=+8 deg.

According to the point that viscousity becomes significant where there is a shear layer, using a viscous solver will lead to better predictions than those of inviscid solvers. Comparisons of the inviscid and viscous results indicate that inclusion of viscosity affects the pressures and blade airloads, especially for transonic tip Mach number cases showing strong shock-induced separations [19]. From an industrial point of view, the viscous effects have little contribution to blade loading, especially in a subsonic regime, so to alleviate time and costs, Euler solution would be sufficient [20]. According to Fig's 9-10, it is obvious that our calculated results are in good agreement with experimental measurements. The present numerical results are in good agreement with the experimental data and they represent an improvement over the previously published Navier-Stokes results that used a simple wake model. The good agreement of the surface pressures predicted by the Euler method with those of Navier-Stokes results seems to suggest that the details of surface flow, including separation and tip vortex details, are not important for predicting airloads. But in transonic cases, the viscous solution is suggested to be used.

At this stage, after methodology validation, the second case simulation which was introduced previously is presented in the following section.

7 Computational Details for Second Case

Calculation for the second case is made for a helicopter including a main/tail rotor and body configuration. The motivation was to calculate the main rotor blade loadings and flow field affected by interaction between the main rotor, tail rotor and body. There are lots of other achievements of this simulation such as body airload prediction, helicopter performance calculation and study of flow interaction. The simulation is done for hovering condition using MRF and Dynamic Mesh approaches. Forward flight considerations of numerical simulation are in progress by authors and will be supported by upcoming papers. Table 1 presents the information about the geometrical and flight condition of the case. For validation of the numerical method, a hovering helicopter flight test is performed.

Table 1. Geometrical Information with Tip Mach number.

Number of blades	2
Tip Mach number	0.69
Rotor diameter	15.24 [m]
Blade chord	0.8382 [m]
Blade twist	-8 deg
Gross Weight	6200 [kg]
Main rotor angular velocity	300 M

7.1 Flight Test Measurements

Parallel to this phase, some fight measurements were conducted including beamwise, chordwise and torsional moments with additional main rotor shaft twisting moment. These measurements were done by bounding strain gauges on proper positions along the blade and a measuring system that enables digital recording of measured parameters during the tests [21]. To get a reliable measurement, calibration was performed within the range of load values expected during the operation of helicopter assemblies or components under test. Forces were applied to the structural component of the helicopter using weights and hydraulic actuators and, then, they were unloaded. Next, the values of electrical signals at each load level were read. After the calibration results became repeatable, we concluded that calibration is satisfied. In flight condition, blades take special angles in order to balance the weight and stay in hover. It means that, for this weight and flight condition, there is a specific motion and position of blades. With data available to compare our results, blade motions including feathering and flapping angles were measured by mounting potentiometer on desired positions [21]. Lead and lag motion was neglected. Fig's 1-12 show the flapping (on blade-hub connection) and feathering (relative to 0.7R) angle variation in time as well as their Fourier Transform in one rotor revolution, respectively. As seen in these figures, the frequency of flapping and feathering is about 5 Hz which is the same as that of rotor rotational frequency. Because of a steady condition and relatively low blade angles fluctuations, the average values of flapping and feathering are entered into our computer model considering initial 2 deg cone angle. For easy meshing, configuration of the body is made more smoothed and as body investigation is not our major purpose, it will not be so problematic. It should be mentioned that hovering flight test data gathering is more difficult than that of forward flight.

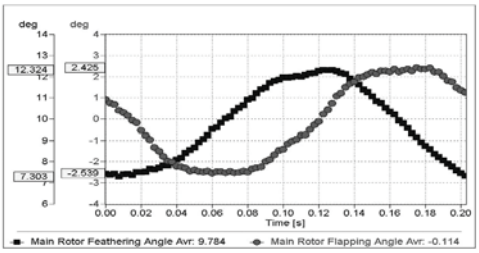

Figure 11. Main Rotor Feathering and Flapping Variation in Time Obtained from Flight Test during one rotor revolutions.

The reason can be found in environmental effects like wind and CG variations due to fuel consumption and any other agents making it difficult to stabilize the helicopter in hover.

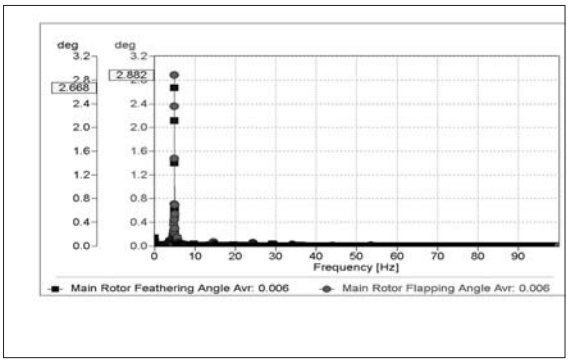

Figure 12. Fourier Transform of Flapping and Feathering Motion Obtained from Flight Test during 100 Rotor Revolutions

To get accurate data, the wind speed should tend to move toward zero but, in reality, it is nearly impossible. To show data gathering to be independent of environmental effects, fig.13 presents variation of flapping and feathering in time during 100 rotor revolutions.

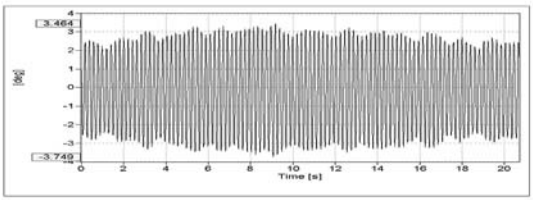

(a)

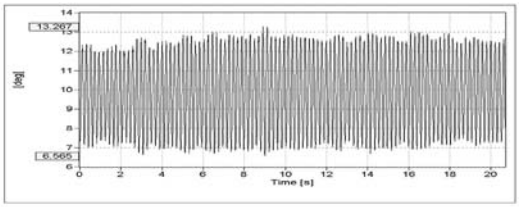

(b)

Figure 13. Blade (a) Flapping and (b) Feathering angles variations for 100 rotor revolutions.

7.2 CFD Simulations

For CFD calculations, hybrid grid topology (structured for near wall region and unstructured for far away region) is made to save CPU and time resources. Three zones including two rotating zones for the main rotor and tail rotor and one stationary zone for the body are made. Interfaces between these zones are assumed to be interior. A mesh density of nearly 3 million cells is chosen after a grid independence study. Structured surface grid points with boundary layer mesh is made for the main rotor which is our major interest. For tail and body surfaces, triangular grids are applied without boundary viscous meshes.

Fig's. 14-16 show the geometrical model of the main rotor blades, body and main/tail rotor configuration, and sectional grid view of the main rotor blades respectively.

MRF simulation as a steady solution along with Dynamic Mesh as an unsteady solution was performed through an implicit steady/unsteady finite volume, and second order upwind solver including mesh motion capabilities for hovering a helicopter. A steady solution was used as the initial solution for the unsteady solver. Then, a few very small time-steps, which were gradually increased to a constant 100 time-steps per revolution, were utilized. For hovering rotor solutions, once sufficient points are used to capture enough turns of the wake, the solution does not converge to a steady state solution; rather, it exhibits oscillatory wakes. This agrees with the results of other published studies using less diffusive formulations, theoretical stability analysis, and experiments. This causes steady solution residuals to fluctuate by iteration.

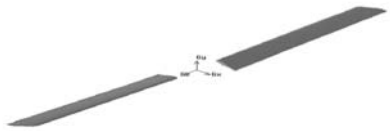

Figure 14. Geometry of Main Rotor Blades

Figure 15. Body Main/Tail Rotor Configuration

Fig's. 17-19 show the velocity pathlines and contours obtained by MRF approach. Interaction between the main and tail rotor is shown and, especially, the well-known contraction of the wake is predicted properly. Experimental data for rotors in hover, for example ref-

erences [22, 23], have suggested the wakes are actually unsteady. This has been confirmed by theoretical stability analyses [24], which imply a hovering rotor wake is fundamentally unstable with several unstable modes. Other simulation methods, for example free-vortex or free-wake [25] or vorticity transport methods, with low inherent dissipation, have also shown evidence of unsteady hover wakes, confirming the theoretical and experimental data. For wake capturing, we need not only high order CFD solver but also high grid density.

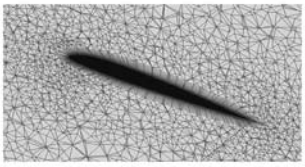

Fig. 16 Sectional grid points with boundary layer viscous grids.

As we are not interested in wake capturing but eager to predict airloads and according to our conclusion in section 5, details of surface flow, including separation and tip vortex details, are not very important for predicting airloads, our calculation should be acceptable.

Figure 17. Pathlines Colored by Velocity Magnitude (m/s) Obtained by MRF.

Figure 18. Contours of Velocity Magnitude (m/s) Obtained by MRF- Side View.

Fig's. 20-21 show the streamlines colored by the velocity magnitude calculated by Dynamic Mesh approach. To validate the calculation procedure, comparisons of thrust as an out-of-plane force and torque as an in-plane force of the main rotor blade are performed.

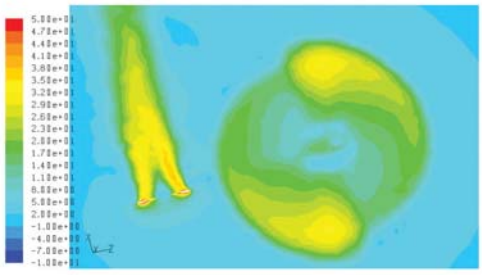

Figure 19. Contours of Velocity Magnitude Obtained by MRF- Top View (m/s).

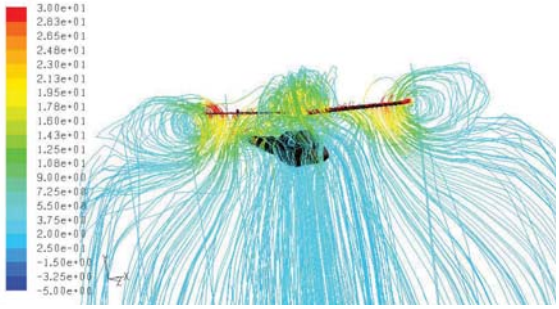

Figure 20. Main Rotor Streamlines Colored by Velocity Magnitude (m/s) – Dynamic Mesh Approach.

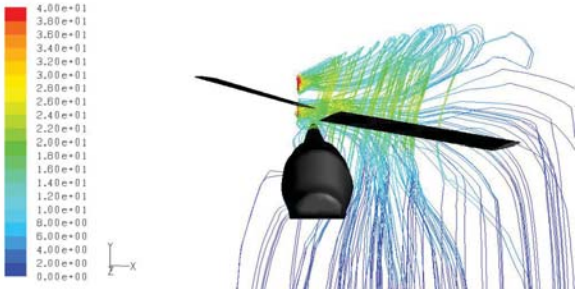

Figure 21. Tail Rotor Streamlines Colored by Velocity Magnitude – Dynamic Mesh.

The thrust value of the main rotor blade is calculated through integration of pressure distribution on and viscous contribution to the blades. Table 2 presents the thrust values obtained from inviscid and viscous calculations. Theoretically, as the helicopter is in hover, to balance the weight, blades should produce an amount of force equal to helicopter gross weight plus body frame drag due to rotor downwash. This amount of drag force is approximately equal to 5 percent of the rotor thrust. As the helicopter gross weight is 62000 (N), body frame drag force will be around 3100 (N). Adding these two values gives the reference thrust value of the main rotor blades.

Table 2. Main Rotor Blades Thrust comparison.

Main rotor blades thrust (N)					
Grid Density (million cells)	Viscous Solution		Inviscid Solution		Ref. Value
	MRF	Dyna. mesh	MRF	Dyna. mesh	
0.8	58850	61023	58520	62535	65100
1.5	63086	64756	62963	65784	65100
3	63397	64955	63007	66153	65100

Grid study of the solution indicated in the table is conducted by the main rotor blades' surface adaption. Table 3 shows the comparisons of the main rotor in-plane calculated force with main rotor shaft twisting moment which is measured during flight test [21]. Figure 22 indicates the main rotor mast twisting variation in 50 revolutions of the rotor which is obtained during the flight test. Due to interactions of the main rotor-body-tail rotor, an amount of mast twisting moment fluctuates by time and has an unsteady trend. To have comparison, the average value of mast twisting moment is chosen.

Table 3. Main Rotor In-plane Force Comparison.

Main rotor blades In-plane Force (N)					
Grid Density (million cells)	Viscous Solution		Inviscid Solution		Measured Value
	MRF	Dyna. mesh	MRF	Dyna. mesh	
0.8	37057	39252	36824	39187	40562
1.5	42091	41550	41993	41365	40562
3	42328	41900	42237	41733	40562

So, up to this point, we predict aerodynamic loads. Next, we present moment distribution along the main rotor blade matching with the measured data.

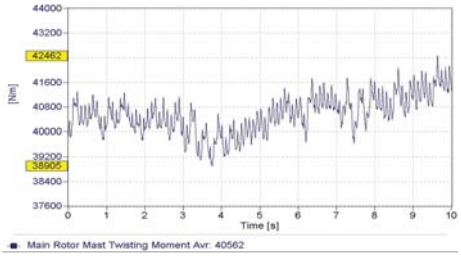

Figure 22. Main Rotor Mast Twisting Moment during 50 Rotor Revolutions (Flight Test) [21].

8 Structural Modeling

After gaining aerodynamic loads of the main rotor blades, a finite-element model of the blade is made assuming a beam with the definition of blade mass distribution and beamwise, chordwise and torsional stiffness for each element. Airloads along with centrifugal forces are applied on the model and moment distribution is calculated. In order to calculate c the entrifugal force, the blade is cut into some equidimentional parts. Multiplying the mass of each part by its radius, by its angular velocity squared, the centrifugal force of that part will be achieved. Figure 23 shows beamwise bending moment distribution.

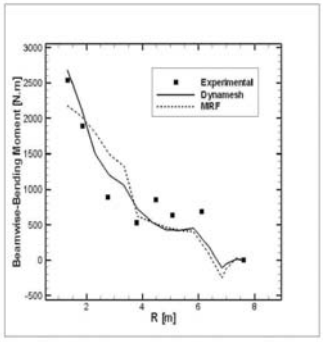

Figure 23. Beamwise Bending Moment Distribution along Blade (Flight test and calculation).

The figure illustrates robustness of Dynamic Mesh on predicting beamwise bending moment distribution. There are some deviations from flight test data that are expectable. As seen in Fig. 11, an angle of attack variation of about 3 degrees will surely affect the aerodynamics of the blade. In addition, flapping motion has an aerodynamic effect equivalent to a reduction of the blade angle of attack; in other words, up-flapping has the same meaning as angle of attack reduction and

down-flapping has the meaning the same as angle of attack increase. As we didn't cover this subject in our simulation, there should be some deviation originating from this point. Also aeroelastic deformations affect the blade aerodynamics. One of the outstanding Dynamic Mesh approach applications is in modeling deformable objects. During hover flight, there is little aeroelastic deformation which can be neglected, as we did. But in forward or clime or descent flight conditions, these deformations become significant. That is because, in forward flight, due to lift dissymmetry, rotor trims itself by flapping blades.

9 Conclusion

An implicit unsteady upwind solver, including mesh motion approach, is applied to simulate a helicopter, with body, main rotor and tail rotor in hover flight. The discretization is based on a second order finite-volume approach with fluxes given by the Roe's scheme. Discretization of Geometric Conservation Laws (GCL) is devised to solve three-dimensional flows on arbitrary moving grids. In order to study wake details, low diffusive methods like free vortex or vorticity transport methods are suggested, because dissipative upwind solver along with dissipative RANS turbulent models will affect the flow-filed vortices and fail to capture the wake truly. By increasing gird density to capture rotor wake, CPU requirements and costs will increase. However, by making use of high order CFD methods, the problem would be overcome to some extent. The good agreement of the surface pressures predicted by the Euler method with those of Navier-Stokes results seems to suggest that the details of surface flow, including separation and tip vortex details, are not important for predicting airloads. So, it is possible to predict the blade spanwise load distribution without accurate vortex location and wake capturing. The chordwise loading is profoundly altered by vortex trajectory and dynamic forces contribution which did not meet the flight test data. Using moving mesh approach is the first step toward deforming body considerations and more physical representation of flow field. To gain more accurate results, it is suggested to couple the unsteady CFD methods with CSD (Computational Structural Dynamic) in loose or full form.

10 Acknowledgment

The authors thank HESA for its participation in performing flight test measurements.

11 References

1. Conlisk, A.T., "Modern Helicopter Rotor Aerodynamics,progress in aerospace sciences", pp. 419-476, 2001.

2. Hsu, A.T., and Wu, J.C., "Vortex flow model for the blade-vortex interaction problem", *AIAA J*., Vol.26, No.5, pp. 621-623.

3. Felker, F.F., Quackenbush, Bliss, T.R., and Light, J.S., "Comparisons of predicted and measured rotor performance in hover using a new free-wake analysis", The 44th Annual Forum of the American Helicopter Society, Washington, DC, June 16018, 1988.

4. Morino, L., and BharadvaJ, B.K., "Two methods for viscous and inviscid free-wake analysis of helicopter rotors", CCAD-TR-85-04-R, Boston University, 1985.

5. Kocurek, J.D. and Tangler, J.L., "A prescribed wake lifting surface hover performance analysis", *J. Am. Helicopter,* (1977.

6. Landgrebe, A.J., "An analytical and experimental investigation of helicopter rotor hover performance and wake geometry characteristics, U.S. Army Air Mobility Research and Development Laboratories", Moffett Field, CA, USAAMRDL TR-71-24, June 1971.

7. Caradonna, F.X., Desopper, A. and Tung, C., "Finite-difference modeling of rotor flows including wake effects", The 8th European Rotorcraft Forum, Aix-Provence, France, Paper 2.7, Aug. 1982.

8. Egolf, T.A. and Sparks, S.P., "Hovering rotor airload prediction using a full potential flow analysis with realistic wake geometry", The 41st Annual Forum of the American Helicopter Society, Ft. Worth, TX, May 1985.

9. Aggarwal, R., and Deese, J., "Euler calculation for flow field of a helicopter rotor in hover", AIAA 4th Applied Aerodynamics Conference, San Diego, CA, June 1986.

10. Sankar, N.L., Wake, B.E., Ruo, S.Y., and Malone, J.B., "Numerical solution of unsteady rotational flow past fixed and rotary wing configurations", NASA CP-3022 (1989) 35 l-374.

11. Srinivasan, G.R., Baeder, J.D., Obayashi, S., and McCroskey, W.J. "Flowfield of a lifting hovering rotor - A Navier-Stokes simulation", NASA TM-102862.

12. Allen, C.B., "Parallel Solution of Lifting Rotors in

Hover and Forward Flight", *International Journal For Numerical Methods In Engineering*, Vol.55, pp. 15-27, 2006.

13. Allen, C.B., "Convergence of Steady and Unsteady Formulations for Inviscid Hovering Rotor Solutions", *International Journal For Numerical Methods In Engineering*, Vol.41, pp.931-949 (2003).

14. Hu, H., "Application of multigrid CFD methods to rotor analysis, Proc. AHS 2nd hit. Aeromechanics Specialists", Conference, Bridgeport, Connecticut, October 11-13, 1995, American Helicopter Society, pp. 659-667.

15. Conlisk, A.T., "Modern Helicopter Rotor Aerodynamics, progress in aerospace sciences", Vol. 37, pp 419-476 ,2001.

16. FLUENT 6.3.26 User's Guide, Fluent Inc.Lebanon, NH 03766, USA, 2006.

17. Thomas, P. D. and Lombard, C. K., "Geometric Conservation Law and Its Application to Flow Computations on Moving Grids", *AIAA Journal*, Vol. 17, No. 10, 1979, pp. 1030 1037.

18. Caradona, F..X., Tung, C., "Experimental and Analytical studies of a model helicopter in hover", USAAVRADCOM TR-81-A-23.

19. Kang, H. J., and Kwon, O. J., "Unstructured Mesh Navier-Stokes Calculations of the Flow Field of a Helicopter Rotor in Hover," *Journal of AHS*, January 2002.

20. Hassanzadeh, D., Mostofizadeh, A. Mirsaeedi, S.A., Sarabi, S., "Parallel turbulence solution of 3D helicopter flowfield in hover", (aero2010-Tehran).

21. "Composite Blade Design and Manufacturing Department", HESA documentation.

22. Landgrebe, AJ., "The wake geometry of a hovering rotor and its influence on rotor performance", *Journal of the American Helicopter Society* 1972, Vol. 17, No. 4, pp 2–15.

23. Tangler, J.L., Wohlfeld, R.M., Miley, S.J., "An experimental investigation of vortex stability, tip shapes, compressibility, and noise for hovering model rotors", NASA CR-2305, 1973.

24. Gupta, B.P., "Loewy RG. Theoretical analysis of the aerodynamic stability of multiple, interdigitated helical vortices", *AIAA Journal*, 1974.

25. Bhagwat, M.J., Leishman, J.G., "On the aerodynamic stability of helicopter rotor wakes", Proceedings of the 56th Annual AHS Forum, Virginia Beach, VA, May 2000.